Preprint of: Paweł Ziółkowski, Dariusz Mikielewicz, Piotr Klonowicz, Łukasz Witanowski (2024). High-speed multi-stage gas-steam turbine with flow bleeding in a novel thermodynamic cycle for decarbonizing power generation. RENEWABLE ENERGY, vol. 237, part B, 121655. **https://doi.org/10.1016/j.renene.2024.121655**

# High-speed multi-stage gas-steam turbine with flow bleeding in a novel thermodynamic cycle for decarbonizing power generation

**Paweł Ziółkowski[1,*], Łukasz Witanowski[2], Piotr Klonowicz[2], Dariusz Mikielewicz[1]**

[1]Gdańsk University of Technology; Faculty of Mechanical Engineering and Ship Technology; Narutowicza 11/12; 80-233 Gdańsk; Poland, pziolkowski@pg.edu.pl

[2]Turbine Department, Institute of Fluid-Flow Machinery, Polish Academy of Sciences, ul. Fiszera 14, 80-231 Gdańsk, Poland,

**Abstract**

In the global pursuit of sustainable energy and reduced carbon footprints, advances in power generation techniques play a crucial role, not only in meeting the ever-increasing energy demands but also in ensuring that environmental standards are maintained and that the health of our planet is prioritized for future generations.

In the ongoing quest for sustainable energy solutions, novel high-speed multi-stage gas-steam turbine models were designed to address the challenge of decarbonized power production. The thermodynamic parameters were adopted on the basis of the negative carbon dioxide gas power plant cycle relying on the following main devices, namely: wet combustion chamber, spray-ejector condenser, sewage sludge gasifier and gas-steam turbine. The peculiarities of the present system make the turbine the link of three important devices and its parameters affect the entire thermodynamic cycle. Therefore, it is reasonable to carry out dedicated novel in literature CFD calculations that also take into account the bleeding of the medium for the gasification process.

Two distinct turbine models were introduced: a two-stage turbine achieving speeds of 95 000 rpm with an efficiency of more than 80%, and a five-stage turbine reaching 40 000 rpm with an efficiency of less than 70%. A design assumption of a bleed pressure of 100 kPa and a mass flow rate of 0.1 kg/s was adopted for both models. Computational simulations were utilized, and the turbine stages were selected with the aim of reducing energy losses. Through this work, a significant step towards a carbon-negative future using high-speed turbine technologies was demonstrated, laying the groundwork for further advancements in the field.

**Keywords**: multi-stage axial turbine, high-speed, carbon capture, negative carbon dioxide emissions power plant (nCO2PP)

* Corresponding author. E-mail address: pawel.ziolkowski1@pg.edu.pl (P. Ziółkowski)

## Nomenclature

| | | | |
|---|---|---|---|
| $\overleftrightarrow{d}$ | - | Deformation rate | [1/s] |
| $e$ | - | Specific energy | [m$^2$/s$^2$] |
| $h$ | - | Specific enthalpy | [m$^2$/s$^2$] |
| $\vec{g}$ | - | Mass forces | [m/s$^2$] |
| $\overleftrightarrow{I}$ | - | Unit tensor (Gibbs' idemfactor) | - |
| $M_m$ | - | Average molar mass | [kg/mol] |
| $\vec{n}$ | - | Normal vector | [-] |
| $p$ | - | Pressure | [Pa] |
| $R$ | - | Individual substance constant | [J/(kgK)] |
| $\vec{q}$ | - | Heat flux | [W/s$^2$] |
| $\overleftrightarrow{r}$ | - | Reynolds' turbulent stress (momentum flux) | [Pa] |
| $T$ | - | Temperature | [K] |
| $\vec{T}$ | - | Torque | [Nm] |
| $\overleftrightarrow{t}$ | - | Total momentum flux | [Pa] |
| $\vec{v}$ | - | Velocity | [m/s] |
| $X_m$ | - | Mole fraction of component *m* | [-] |
| $Y_m$ | - | Mass fraction of component *m* | [-] |
| $\overleftrightarrow{\tau}$ | - | Momentum flux of viscous stress | [Pa] |
| $\overleftrightarrow{\tau}^c$ | - | Total irreversible momentum flux | [Pa] |
| $\mu$ | - | Dynamic viscosity | [Pas] |
| $\rho$ | - | Density | [kg/m$^3$] |
| $\vec{\omega}$ | - | Rotational speed | [rpm] |

*Abbreviations:*

C - compressor,

| | |
|---|---|
| CC | - combustion chamber, |
| CCS | - carbon dioxide capture and storage systems, |
| CCU | - Carbon Capture Unit, |
| CES | - Clean Energy Systems, |
| CFD | - Computational Fluid Dynamics, so-called three-dimensional description of unknowns parameters of the power plant devices |
| CHE | – cooling heat exchanger, |
| SEC | – spray-ejector condenser, |
| G | – electric generator, |
| GT | – gas turbine, |
| HE | – heat exchanger, |
| P | – pump, |
| S+CHE | - condensate-cooler heat exchanger and separator, |
| WCC | – wet combustion chamber |

## 1. Introduction

According to empirical data from NASA [1,2], July 2023 emerged as a thermodynamic anomaly, setting the record for the hottest month ever documented (Fig. 1). The temperature anomaly for that month surpassed previous July readings by 0.24°C and stood at 1.18°C above the average July temperatures noted during the 1951-1980 baseline period. This data accentuates the urgency of the engineering objectives outlined in the Paris Agreement. Grounded in this pact, a firm thermodynamic target has been committed to by the global community: the attenuation of anthropogenic factors to ensure that the average global temperature does not rise by more than 1.5°C from pre-industrial levels. Beyond its geopolitical ramifications, this agreement has galvanized the engineering sector, catalyzing a wave of technological breakthroughs.

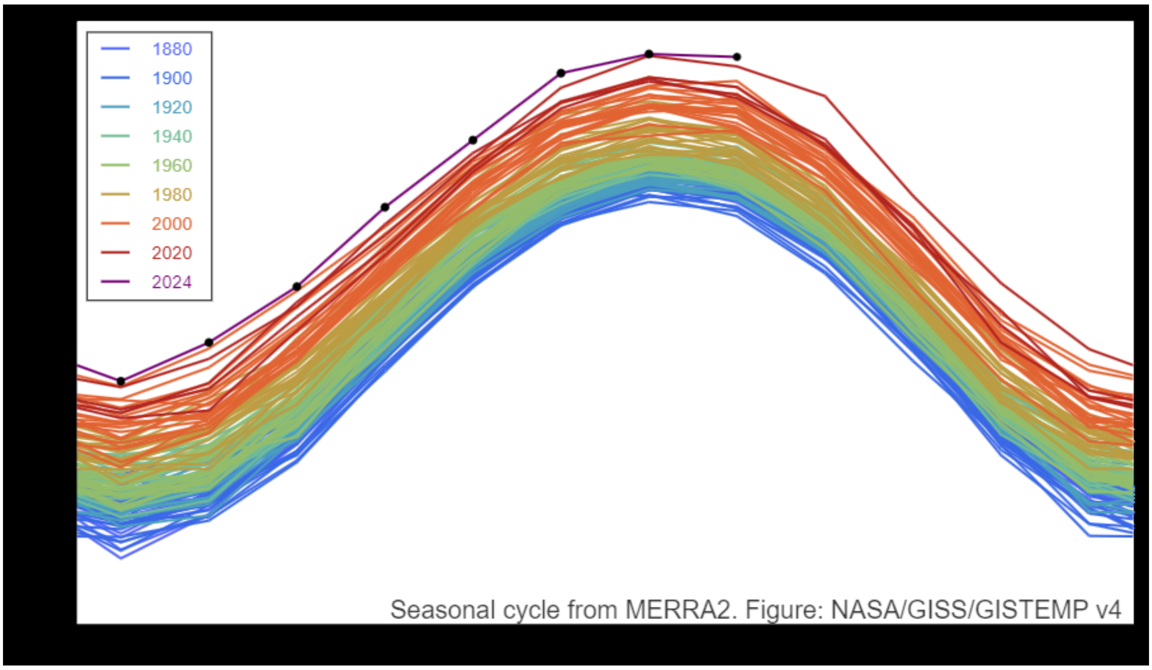


**Fig. 1** Global temperature anomalies for every July since the 1880s, based on NASA's GISTEMP analysis. Anomalies reflect how much the global temperature was above or below the 1951-1980 norm for July [1,2].

The unprecedented temperature anomaly accentuates the need for efficient renewable energy utilization. A key study highlights advancements in energy system modelling for solar and wind power, emphasizing the need for higher temporal resolution to address their intermittent nature [3]. For solar energy, stochastic and non-dimensional approaches are effective for data downscaling. However, wind speed data downscaling is more complex, with current trends favoring a combination of meteorological reanalysis and stochastic methods. Wind energy's role in decarbonizing grids becomes crucial, with projections suggesting it might account for 40% of energy generation in many regions [4]. However, this increase leads to challenges like mismatches between generation and grid demand, causing wind energy devaluation. This is measured by the Value Factor, reflecting a potential 60% loss in revenue due to intermittency, as seen in US grids with high wind shares. Mitigation strategies include enhancing grid transmission, government subsidies, and long-duration energy storage. A proposed grid classification system based on the Net Value Factor (NVF) aims to optimize wind energy systems, balancing costs with revenue. These approaches are essential for effectively integrating wind power into increasingly decarbonized grids. Wind energy's role in grid decarbonization is complemented by photovoltaic (PV) advancements. Accurate PV performance forecasts, essential for grid integration, are challenged by spectral influences, with errors up to 14% in technologies like polycrystalline silicon [5].

Spectral correction functions (SCFs) are employed to address this, with methods based on direct spectral parameters like average photon energy proving more accurate than proxy-variable methods. A decision-making framework guides PV modelers, considering climate and system specifics, to improve forecasting accuracy, crucial for grid efficiency. Alongside wind energy and PV advancements, the development of Multi Energy Systems (MES) for efficient power management is gaining prominence [6]. Key to MES optimization is addressing technical constraints and uncertainties, with a focus on incorporating thermal networks and storage. Recent studies emphasize practical optimization with clear mathematical formulation and solver choice, balancing descriptive accuracy and ease of implementation. This approach aids in integrating diverse energy sources into the grid effectively.

The global assessment of run-of-river hydropower potentials, considering technical, economic, and environmental constraints, reveals significant prospects for future energy development. Utilizing detailed global runoff data and Digital Elevation Models (DEMs), the authors' work [7] estimates a global exploitable hydropower potential ranging from 5.42 to 39.56 (PWh/yr), depending on flow dependability. This highlights the importance of precise hydrologic and topographic data in identifying sustainable and economically viable hydropower sites amidst increasing energy demands.

A significant challenge in energy systems is the management of waste heat, showing that 72% of global primary energy consumption is lost in post-conversion, mainly in electricity generation, transportation, and industry [8]. Much of this waste heat is available at temperatures below 100 °C, posing an opportunity for improved energy efficiency. The study proposes a novel approach to estimate this potential globally, addressing the temperature distribution and exergy content of waste heat. While there are obstacles like technical constraints and financial barriers, solutions such as the Organic Rankine Cycle (ORC) [9–11], Organic Flash Cycle [12,13] and heat pumps [14–16] are being explored for low-grade waste heat recovery. Efficient utilization of waste heat, could significantly enhance energy systems' sustainability [17].

The fight against global warming necessitates a multifaceted approach, incorporating not only renewable energy sources and systems that effectively utilize waste heat but also pioneering technologies like the negative carbon dioxide emissions gas power plant ($nCO_2PP$) [18]. Advancements in negative carbon dioxide emissions power plant ($nCO_2PP$) technology utilize sewage sludge for environmentally beneficial electricity generation [19]. A mathematical model is developed to estimate thermodynamic parameters, focusing on the interaction between gasification and gas-steam turbine operations. The integration of the gasification reactor with the turbine model significantly enhances system efficiency. This method shows potential in achieving negative $CO_2$ emissions and suggests that increased turbine bleed pressure can further optimize power generation efficiency, contributing to sustainable and environmentally friendly energy solutions. An important element of this system is the turbines, or more specifically, their efficiency, which greatly impacts the efficiency of the entire cycle. These types of turbines are exposed to extreme operating conditions due to the parameters of the working medium. The temperature of the working medium often exceeds 1000°C, which is extremely important to consider when designing these types of devices.

The authors of the paper [20] examine heat transfer in a high-speed turbine rotor shaft cooling passage using Computational Fluid Dynamics (CFD) and supercritical CO2. Key aspects studied include coolant temperature, heat transfer coefficient, and the effects of clearance, mass flow rate, shaft rotational speed, and temperature. Findings reveal that coolant temperature and heat transfer coefficient are minimally affected by radial clearance, which is significant for turbine design. The study also shows that convection heat transfer is much higher than frictional heat transfer, indicating a dominant role in cooling efficiency. Utilizing NIST real gas data for CFD simulations, the research finds that convection heat transfer values predicted by CFD are significantly higher than those predicted by correlation methods. These insights are crucial for optimizing high-speed turbomachinery, particularly in improving turbine cooling systems. Developing a high-temperature turbine for supercritical organic Rankine cycle (SORC) systems, a radial-axial two-stage coaxial design is optimized using Siloxane MM as the working medium [21]. This turbine achieves an isentropic efficiency of 86.55% at an expansion ratio of 15.37 and is suitable for medium to high temperature ORC systems. The design, validated through 3D simulations, demonstrates high efficiency and adaptability under various operational conditions, representing a significant advancement in high-temperature turbine technology for renewable energy systems. In another analysis [22], finite element methods were used to analyze stress and strain dynamics in the intermediate-pressure steam turbine rotor. The study aims to identify critical regions and assess their fatigue life under various operational conditions. Notably, the heat grooves in the balance piston were found to be prone to cracking. The Prager–Ziegler kinematic hardening model is validated as a reliable tool for predicting both strain amplitudes and fatigue life, closely aligning with field and non-destructive test data. A comprehensive review of cooling technologies highlights advancements in both the scientific and engineering aspects of cooling technology [23]. For numerical simulations, the RANS approach remains the preferred method, while enhanced measurement tools offer valuable experimental insights. Significant progress has been achieved in understanding the effects of rotational forces on heat transfer. Cooling designs have evolved, particularly with promising innovations like lamellar and micro-scale cooling. Research on disk and cavity cooling specifically targets rotor-stator systems and the positioning of air injection.

With respect to turbine flow systems, there is no work taking into account the nature of the flow in the area of bleeders, and if CFD analysis is carried out, turbine outlets are the subject to analysis [24–27]. Typically, in the context of reducing exhaust loss, it is important to include the interaction between the last stage and the exhaust diffuser. In this work, a simplified bleeding channel was introduced, so this is an advantage of this work because, in addition to changing the flow rate, the influence of the flow diffuser is visible. It is also worth mentioning the fact that this work is new also in terms of flow testing in turbine design, because, as the examples show [28–31], the analyzes are usually conducted in the context of a channel without changing the flow mass.

In other words, CFD analysis performed in this article, cover a literature gap in respect to bleed for 3D geometry in wide range parameters. The findings from this study are significant not just for their immediate technical implications but also for their broader impact on sustainable energy production. The research presents a compelling case for the feasibility and effectiveness of high-temperature turbines in $nCO_2PP$ systems, providing a template for future advancements in this field. The meticulous analysis of stage power, efficiency, and the influence of various operational parameters offers invaluable guidance for the structural design and optimization of future turbine systems.

The primary objective of this study is to design and compare two novel high-speed, high-temperature turbine configurations while precisely determining the bleed pressure, with a target of approximately 100 kPa. These turbines exhibit variations in the number of stages and rotational speeds while sharing a common characteristic in terms of inlet and outlet diameters. The turbines presented in this work are intended for utilization within an innovative negative carbon dioxide gas power plant ($nCO_2PP$). The results of this study provide a comprehensive understanding of the effects of varying the bleed level within the range of 0 to 20%, the outlet pressure within the range of 7 to 30 kPa, and the rotational speed within ± 10,000 rpm of the design rotational speed. Furthermore, this research investigates how these parameters impact the overall performance of the turbine.

## 2. Thermodynamic $nCO_2PP$ cycle integrated with gasification

Calculations for the $nCO_2PP$ cycle itself have already been carried out for several power levels with a distinction between several configurations [19,32–37]. Ziółkowski et al papers [32,33] considered a 156 kWe cycle, but without including the gas turbine bleed, and gasification was from an external heat source using steam. In [15], the bleed was fully linked to the nCO2PP cycle, in such a way that the bleed stream reached the gasification reactor, where syngas production took place using a converting agent containing $H_2O$ and $CO_2$. In the aforementioned work [15], the power of the system dropped to 143 kWe due to a reduction in the power given off by the turbine, but this effect did not take into account the change in stage efficiency, which is taken into account by CFD calculations. Much higher capacities were analyzed by Ertesvåg et al. [38] where 2 MWe was considered, which was supposed to correspond to a power plant adapted to a typical wastewater treatment plant producing 10,000 tons of sludge per year. The schematic of the devices operating in the $nCO_2PP$ cycle is shown in Fig.2(a), and in turn the course of thermodynamic processes in the T-s diagram is illustrated in Figure 2(b).

The first points in the cycle can be determined after the fuel and oxygen compressor ($C_{fuel}$, $CO_2$). These direct the fluids to the wet combustion chamber (WCC). In the WCC, combustion takes place with simultaneous injection of water, resulting in a mixture of $CO_2$ and $H_2O$. In order to maintain the temperature of the medium at $T_2$=1100ºC, the injection of water as a coolant is mandatory. The mass flux of water (nodal points $0H_2O$, $1H_2O$ and $2H_2O$, $3H_2O$) is regenerated contributes to the turbine efficiency, which is dependent on the mass flux of regenerated heat.

After the process in the WCC, the exhaust gas expands in the turbines (GT). The exhaust gas is then used to heat water, which is transported to the WCC in heat exchanger (HE1). Part of the flue gas stream is directed to the gasifier (R) and used in the gasification process. An extensive analysis of the impact of thermodynamic parameters in the extraction point on the syngas production process was carried out in [15], where the pressure of the extraction point was in the range of $p_3$=0.7 - 1.6 bar. As a result of the analysis, it was decided to leave the present parameters at the originally established level, namely at a bleed pressure of $p_3$=1 bar and a temperature of $T_3$=672 ºC.

The spray-ejector condenser (SEC) sucks in the exhaust gases from the heat exchanger (HE1). Water is supplied for the intake and condensation process, which comes from the pump ($P_{SEC}$). The presence of motive water, which breaks down into droplets to promote direct contact condensation of the mixture of water vapor and carbon dioxide, namely, enables the process of $H_2O$ condensation and $CO_2$ separation. The uncondensed mixture of water and carbon dioxide SEC goes to the separator with heat exchanger (S+HE2).

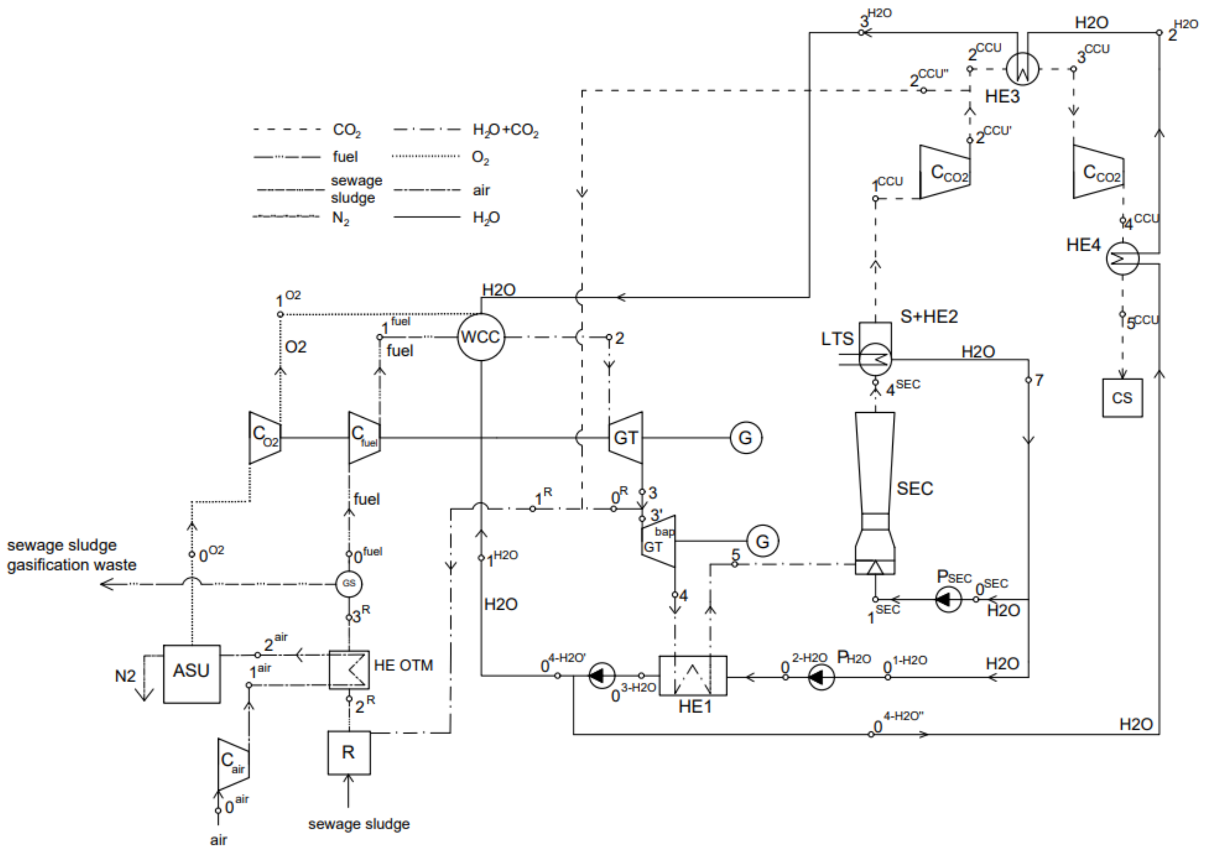


(a)

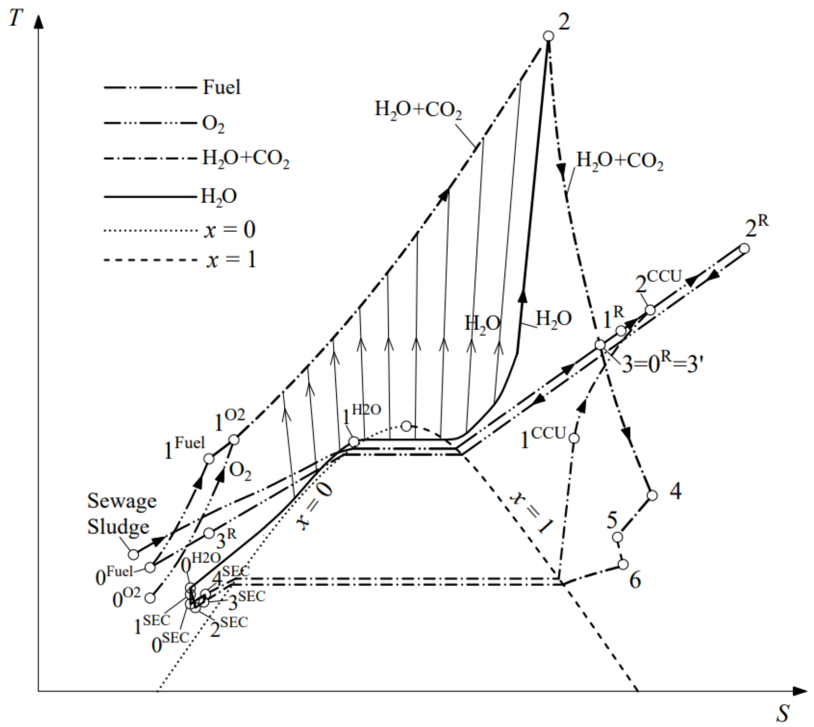


(b)

**Fig. 2** The negative emission $CO_2$ gas power plant ($nCO_2PP$): (a) schematic of the devices operating, where: $C_{O2}$ – oxygen compressor, $C_{fuel}$ – fuel compressor, WCC – combustion chamber, GT – gas turbine, $GT^{bap}$ – low-pressure turbine, HE1 – heat exchanger 1, SEC – spray-ejector condenser, G – generator, $P_{H2O}$ – water pump, $P_{SEC}$ – SEC pump, S+HE2 – separator connected with heat exchanger 2, $C_{CO2}$ – $CO_2$ compressor, HE3 – heat exchanger 3, HE4 – heat exchanger 4, GS – gas scrubber, R – gasifier, ASU – air separation unit [34], (b) thermodynamic transformations in the *T-s* diagram [19].

## 3. Methodology

In this study, two distinct axial turbine designs were developed to meet the specific requirements of a negative carbon dioxide gas power plant integrated with the gasification of sewage sludge [19]. Both solutions (Turbine A and Turbine B) were analysed in an analogous way, namely, first the geometry was created, then mathematical models were used to assess the flow inside the turbine channel, and the final step in the adopted methodology was to change the operating parameters of the turbine.

### 3.1. Geometries and basic assumptions for Turbine A & Turbine B

The primary challenge in designing these turbines stems from the low mass flow rate of 0.1 kg/s, which necessitates careful consideration of specific speed and manufacturing constraints. The first turbine design, referred to as Turbine A, consists of two stages operating at a high speed of 95,000 rpm. This high speed configuration is essential to maintain adequate specific speed values due to the low volume flow, ensuring efficient energy conversion and minimizing aerodynamic losses. The second turbine design, Turbine B, consists of five stages, each operating at a lower speed of 40,000 rpm. The choice of multiple stages at a reduced speed aims to balance aerodynamic performance with manufacturing feasibility, as lower speeds alleviate some of the technological challenges associated with high-speed machines.

A key design assumption for both turbines is the implementation of a turbine bleed at $p_3$=100 kPa. This bleed system plays a critical role in controlling flow characteristics and was instrumental in determining the optimal distribution of enthalpy drop across the turbine stages. The bleed pressure influenced stage loading and reaction levels, allowing for tailored aerodynamic performance in each stage. Another important design consideration was the assumption of equal blade heights at the turbine inlet and outlet. This assumption simplifies the mechanical design and manufacturing processes, facilitates consistent flow conditions throughout the turbine, and reduces the complexity of the flow path geometry.

The turbines are designed to operate under the following process conditions: an inlet total pressure of $p_2$=1000 kPa, an outlet static pressure as low as $p_4$=7 kPa, and an inlet total temperature of $T_2$=1100 °C. The extreme pressure ratio across the turbines presents significant aerodynamic challenges, requiring meticulous design to prevent flow separation and ensure stable operation. The calculated reaction degrees were adjusted to be lower by 10% in each stage for the 5-stage turbine and lower by 20% in each stage for the 2-stage turbine, optimizing the balance between the stator and rotor blade loading. Examples of the turbine geometries are shown in Fig. 3 and Fig. 4, while the design parameters of the turbines are summarized in Table 1.

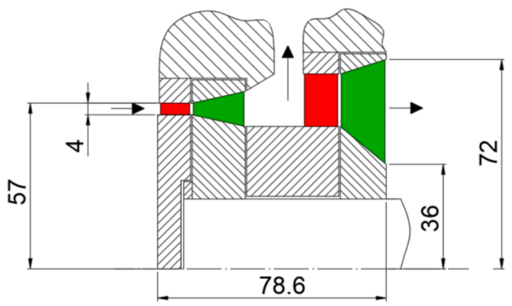


**Fig. 3.** Meridional section of the baseline two stages axial turbine(stator – red, rotor – green).

The preliminary design was conducted using one-dimensional mean-line analysis, incorporating the Traupel loss model [39,40] to accurately estimate aerodynamic losses. The Traupel model accounts for various loss mechanisms, including profile losses due to blade friction, secondary losses from three-dimensional flow effects, tip leakage losses, and trailing edge and exit losses. By integrating this loss model into the design process, a comprehensive assessment of turbine performance was achieved, identifying areas for optimization.

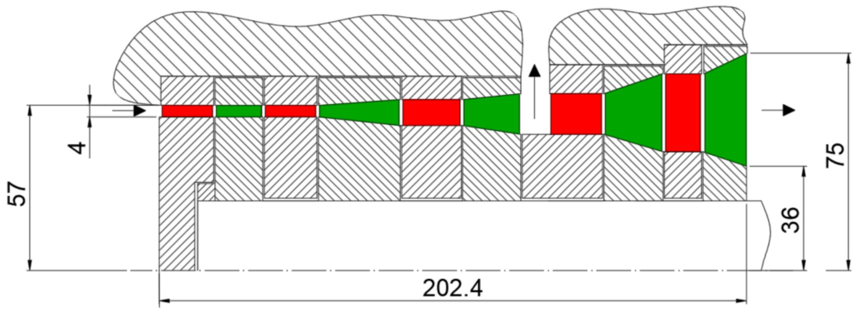


**Fig. 4.** Meridional section of the baseline five stages axial turbine (stator – red, rotor – green).

**Table 1**

Design parameters of turbines.

| *Parameter* | *Unit* | *Turbine A* | *Turbine B* |
|---|---|---|---|
| *Inlet pressure* | *[kPa]* | *1000* | |
| *Inlet temperature* | *[°C]* | *1100* | |
| *Outlet pressure* | *[kPa]* | *7* | |
| *Mass flow rate* | *[kg/s]* | *0.1* | |
| *Working fluid* | *[-]* | *Mixture of:* $H_2$-$CO_2$-$N_2$ | |
| *Rotational speed* | *[rpm]* | *95 000* | *40 000* |
| *Stages number* | *[-]* | *2* | *5* |
| *Bleed pressure* | *[kPa]* | *100* | |

The flow channels of Turbines A and B are presented in Fig. 5 and Fig. 6. The meridional view of the flow expansion (top of Fig. 5) shows a sudden increase in fluid volume especially in the last stage of the turbine. In contrast, a view of the blade profiles and the fluid domain on the peripheral slice (bottom of Fig. 5) illustrates the inflow and outflow angles in the turbine stages. A meridional view of the flow expansion in a five-stage turbine (top of Fig. 6) suggests an orderly growth of the channel cross-section. Then, at the bottom of Fig. 6, there is a view of the blade profiles and the fluid domain on the peripheral slice. However, in order to fully analyze the behavior of the fluid it is necessary to use the mathematical model presented in the next subsection.

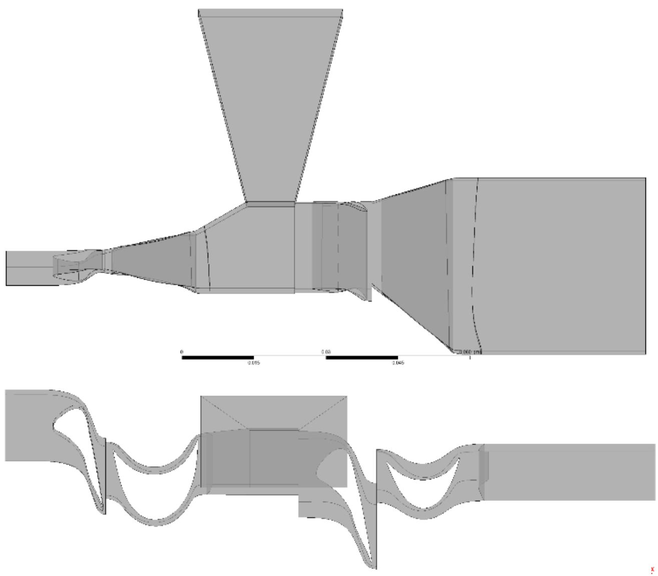

**Fig. 5.** Flow channel of turbine A: two-stage configuration. Meridional view (top) and peripheral slice view (bottom).

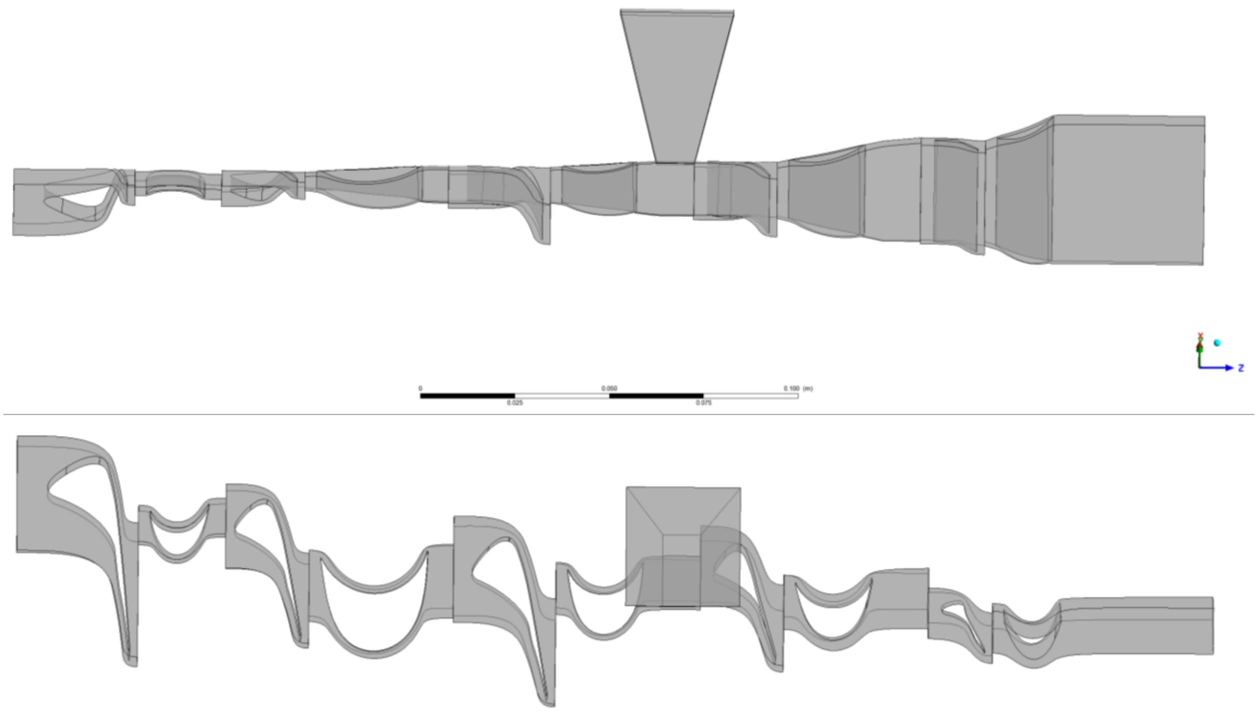

**Fig. 6.** Flow channel of turbine B: five-stage configuration. Meridional view (top) and peripheral slice view (bottom).

### 3.2. Mathematical model for CFD simulations

Subsequent three-dimensional computational fluid dynamics (CFD) analyses were performed to refine the turbine designs and validate the preliminary assessments. The flow domain of each turbine stage was discretized using Ansys Turbogrid software, generating high-quality structured meshes suitable for turbomachinery simulations. Special attention was given to mesh quality parameters to ensure numerical accuracy and convergence. Mesh limits were set on the maximum face angle (165°), minimum face angle (15°), connectivity number (12), maximum volume ratio (10), minimum volume ratio (0), and maximum edge length ratio (500). These parameters were carefully selected based on mesh sensitivity studies to balance computational cost and solution accuracy. The final computational grid for each turbine comprised several million elements, providing sufficient resolution of the flow features within the blade passages. During the grid independence study, computational meshes with up to 5 million nodes per blade-to-blade passage were investigated. It was found that the maximum relative differences in isentropic efficiency between the finest mesh (5 million nodes) and a mesh with 2 million nodes were less than 0.5% (Fig. 7). This negligible difference indicates that the mesh with 2 million nodes is sufficient to accurately capture the flow characteristics, providing a good ratio between computational efficiency and solution accuracy.

The thermal- flow calculations were based on a mathematical model based on a classical system of equations, namely mass, momentum and energy balance. The general mass balance equation is commonly known by the form [41]:

$$\frac{\partial}{\partial t}(\rho) + \mathrm{div}(\rho\vec{v}) = 0 \tag{1}$$

where $\vec{v}$ is the velocity and $\rho$ represents density, $\frac{\partial}{\partial t}$ means derivative in time and div depicts divergenge. Firstly, taking into account different species the sum of mass fractions of components is equal one:

$$\sum_{m=1}^{NS} Y_m = 1 \tag{2}$$

Lower index $m$ indicates the component in the fluid that is assigned the corresponding number $m = 1 \dots NS =$ $H_2$, $CO_2$, $N_2$ . Secondly, the same as for molar fractions:

$$\sum_{m=1}^{NS} X_m = 1 \tag{3}$$

A further governing equation used in CFD calculations is the momentum balance defined as follows [42]:

$$\frac{\partial}{\partial t}(\rho\vec{v}) + \mathrm{div}(\rho\vec{v}\otimes\vec{v}) = \mathrm{div}(\overleftrightarrow{t}) + \rho\vec{g} \tag{4}$$

Where $\vec{g}$ is mass force, $\overleftrightarrow{t}$ represents tensor of momentum flux, and ⊗ means dyadic multiplication. It should be mention that the total momentum flux is given as:

$$\overleftrightarrow{t} = -p\overleftrightarrow{I} + \overleftrightarrow{\tau} + \overleftrightarrow{r} = -p\overleftrightarrow{I} + \overleftrightarrow{\tau}^{c} \tag{5}$$

Total momentum flux is a sum of pressure with Gibbs idemfactor $p\overleftrightarrow{I}$, Reynolds' turbulent flux $\overleftrightarrow{r}$, and tensor of viscous stress defined by Stokes formula [43]:

$$\overleftrightarrow{\tau} = 2\mu\left[\overleftrightarrow{d} - \frac{1}{3}\mathrm{div}(\vec{v}\,)\overleftrightarrow{I}\right] + \mu'\mathrm{div}(\vec{v}\,)\overleftrightarrow{I}, \tag{6}$$

Where $\mu$ means viscosity, $\overleftrightarrow{d}$ is a deformation rate describe by equation:

$$\overleftrightarrow{d} = \frac{1}{2}(\mathrm{grad}\vec{v} + \mathrm{grad}^T\vec{v}) = \overleftrightarrow{d}^T, \tag{7}$$

The constitutive equations for fluid describing the state of real gas was accomplished according information from REFPROP. The total, internal and kinetic energy balance equation in the homogeneous mixture model contains the time variations of the quantity to be balanced, the fluxes of this quantity leaving (or entering) the control region and the source terms [44]:

$$\frac{\partial}{\partial t}(\rho e) + \operatorname{div}(\rho e\vec{v}) = \operatorname{div}\left(\vec{q} + \vec{q}^{t} + \overleftrightarrow{t}\,\vec{v} + \vec{q}^{rad}\right) + \rho\vec{g}\cdot\vec{v} \tag{8}$$

where sum of kinetic and internal energy is $e = \epsilon + \frac{\vec{v}^2}{2}$, turbulent, molecular, and radiative heat fluxes, respectively $\vec{q}^{t}$, $\vec{q}$, $\vec{q}^{rad}$, mechanical energy flux $\overleftrightarrow{t}\,\vec{v}$, and enthalpy of the component per unit mass of the component defined as:

$$h_m = \epsilon_m + \frac{p_m}{\rho_m} \tag{9}$$

Given that the total momentum flux $\overleftrightarrow{t} = -p\overleftrightarrow{I} + \overleftrightarrow{\tau}^{c}$ is divided into an elastic reversible part ($p\overleftrightarrow{I}$, first order derivatives) and a mechanical diffusive part $\overleftrightarrow{\tau}^{c}$, the mechanical momentum flux component $-p\overleftrightarrow{I}\vec{v} = -p\vec{v}$ moves to the left-hand side, hence the equation takes the form

$$\frac{\partial}{\partial t}(\rho e) + \operatorname{div}\left[\left(e + \frac{p}{\rho}\right)\rho\vec{v}\right] = \operatorname{div}\left(\vec{q} + \vec{q}^{t} + \overleftrightarrow{\tau}^{c}\vec{v} + \vec{q}^{rad}\right) + \rho\vec{g}\cdot\vec{v}. \tag{10}$$

The fluid flow in the turbine is adiabatic so we can neglect the components associated with heat flux. The enthalpic formulation uses the relationship as follows:

$$\rho e = \rho h + \rho\frac{\vec{v}^2}{2} - p \tag{11}$$

where sum of kinetic and internal energy is $e = \frac{\vec{v}^2}{2} + \epsilon$. In the literature total enthalpy is described by formula:

$$h^{c} = h + \frac{\vec{v}^2}{2}\,. \tag{12}$$

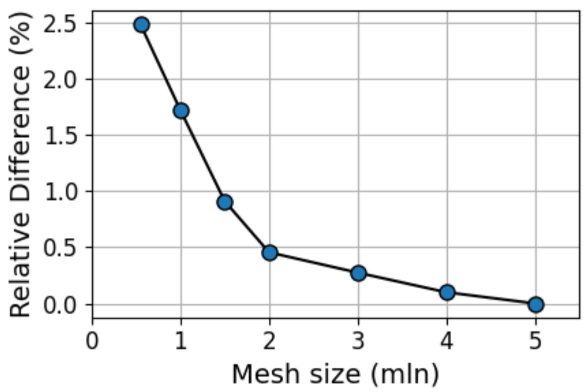


**Fig. 7** Relative difference between mean values of isentropic efficiency obtained on different grids with respect to the finest investigated grid

Steady-state CFD simulations were carried out using Ansys CFX [45], employing the Reynolds-averaged Navier-Stokes (RANS) equations coupled with the k-ω SST turbulence model. The k-ω SST model was chosen for its ability to accurately predict flow separation and turbulence effects in turbomachinery applications. A second-order discretization scheme was applied for both the convective and diffusive terms to enhance the accuracy of the numerical solution.

The working fluid properties were modeled using a real gas equation of state, with thermodynamic and transport properties obtained from look-up tables generated using REFPROP version 10 [46]. The real gas model accounts for the non-ideal behavior of the working fluid at high temperatures and pressures, ensuring accurate prediction of density, enthalpy, and other thermodynamic properties critical to turbine performance. Periodic boundary conditions were applied to the sides of the computational domain to simulate the full annulus behavior using a sector model, thereby reducing computational effort. Since the simulations were steady-state, transient rotor-stator interactions were not modeled. Instead, the frozen rotor approach was employed to approximate the interaction between stationary and rotating components. The frozen rotor method maintains the relative positions of the rotor and stator blades fixed, capturing the circumferential variations of flow properties at the interface without time-averaging. Boundary conditions were specified as follows: total pressure, total temperature, and flow direction were imposed at the turbine inlet; static pressure was specified at the outlet; rotational speed was applied to the rotor domains; and mass flow rate was defined at the bleed outlet.

The flow fields obtained from the CFD simulations were analyzed to assess key performance metrics such as total-to-static efficiency, stage loading, reaction degree, and secondary flow effects. Validation of the proposed approach and the associated computational model took place in authors' preceding work, where the results of CFD calculations were compared with the measurements and construction of real machines [47,48].

### 3.3. Parameter variations and presentation approach

Calculations were performed for various bleed mass flow rates ranging from 0% to 20% of the total mass flow to assess the impact of bleed on turbine performance. Additionally, both turbines were evaluated without bleed at their respective design rotational speeds. Specifically for Turbine A, further analyses were conducted at different rotational speeds and outlet pressures for each selected bleed level to investigate the sensitivity of turbine performance to these operating parameters.

The integral parameter that links the 3D CFD approach to the design calculations is the isentropic total-to-static efficiency which can be described as follows [49]:

$$\eta_{ts} = \frac{h_{2T} - h_{4T}}{h_{2T} - h_{4s'}} \ . \tag{13}$$

where $h_{2T}$ is specific total enthalpy at the inlet to turbine in respect to design approach, $h_{4T}$ and $h_{4s'}$ represents specific total and isentropic enthalpy, respectively, at the outlet from turbine (See Fig 2). As presented in Figure 3, in the case of Turbine A two-stage, the bleed after the first stage corresponds to the bleed in Figures 2 and 3. And in the case of Turbine B multi-stage, on the other hand, the bleed is after three stages, so this definition can easily be referred to a group of stages or to a single stage. Additionally, the isentropic total-to-total efficiency is determined as follows:

$$\eta_{tt} = \frac{h_{2T} - h_{4T}}{h_{2T} - h_{4s'} - \frac{c_4^2}{2}} \ . \tag{14}$$

where, in addition, there is the turbine absolute velocity (velocity in a stationary reference frame) expressed as a variable in terms of 0D.

During the analysis of integral parameters, results related to power were analyzed first. Normalized turbine power is defined as:

$$\mathrm{N}_n = \frac{N_{var}}{N_{without\ bleed}} = \frac{\vec{\omega}\,\vec{T}}{\vec{\omega}\,\vec{T}_{without\ bleed}}. \tag{15}$$

where $\vec{\omega}$ is rotational speed and $\vec{T}$ means torque. $N_{var}$ is turbine power in variable conditions, especially during bleed process. $N_{without\ bleed}$ represents the turbines without bleed. Therefore, the turbine power in most general way described as follows:

$$N_{var} = \vec{\omega}\,\vec{T}. \tag{16}$$

Then, normalized stage power is as follows:

$$\mathrm{N}_{n\;stage} = \frac{N_{var\;stage\;no}}{N_{without\;bleed\;stage\;no}}. \tag{17}$$

where $N_{without\;bleed\;stage\;no}$ represents stage of the turbines without and $N_{var\;stage\;no}$ is stage power in variable conditions in which $no = 1{,}2$ for Turbine A and $no = 1, \dots, 5$ for Turbine B. bleed . However, the power ratio has been defined only for two stage turbine (Turbine A) in the following equation:

$$\mathrm{N}_{stages\;ratio} = \frac{N_{stage\;2}}{N_{stage\;1}}. \tag{18}$$

Furthermore, normalized total-to-static efficiency in turbines can be find as follows:

$$\eta_{ts\;n} = \frac{\eta_{ts\;var}}{\eta_{ts\;without\;bleed}}. \tag{19}$$

where $\eta_{ts\;var}$ total-to-static efficiency in turbines for variable conditions and $\eta_{ts\;without\;bleed}$ represents total-to-static efficiency in turbines for conditions without bleed.

Flow visualization techniques were employed to identify regions of flow separation, high turbulence intensity, and potential loss mechanisms. The results provided valuable insights into the aerodynamic behavior of the turbines under various operating conditions, informing further design refinements.

By integrating detailed aerodynamic modeling, rigorous mesh generation criteria, and comprehensive CFD analyses, the methodology established a robust framework for designing axial turbines operating under challenging conditions of low mass flow rates and high pressure ratios. This approach ensures that the final turbine designs achieve optimal performance while meeting the technological constraints of manufacturing and operation in a negative carbon dioxide gas power plant.

## 4. Results and discussion

### 4.1. Performance analysis under different turbine bleed conditions

A two-stage turbine operating at a speed of 95,000 rpm achieved 122.9 kW with an efficiency of 81.5% (turbine A), while a five-stage turbine achieved 99.5 kW with an efficiency of 62.7% (turbine B). The use of a bleeder significantly changes the turbine parameters, as presented in the section below.

The normalized turbine power and normalized total-to-static efficiency are presented in Fig. 8-8. In the result figures, the dashed line represent results obtained with turbine A, and the dashed dot line represent the results with turbine B. The power drop in turbine B is greater, despite the higher increase in normalized efficiency. However, this increase does not compensate for the significantly lower base efficiency of turbine B, especially considering the potentially lower efficiency of the stages located immediately after the bleeder.

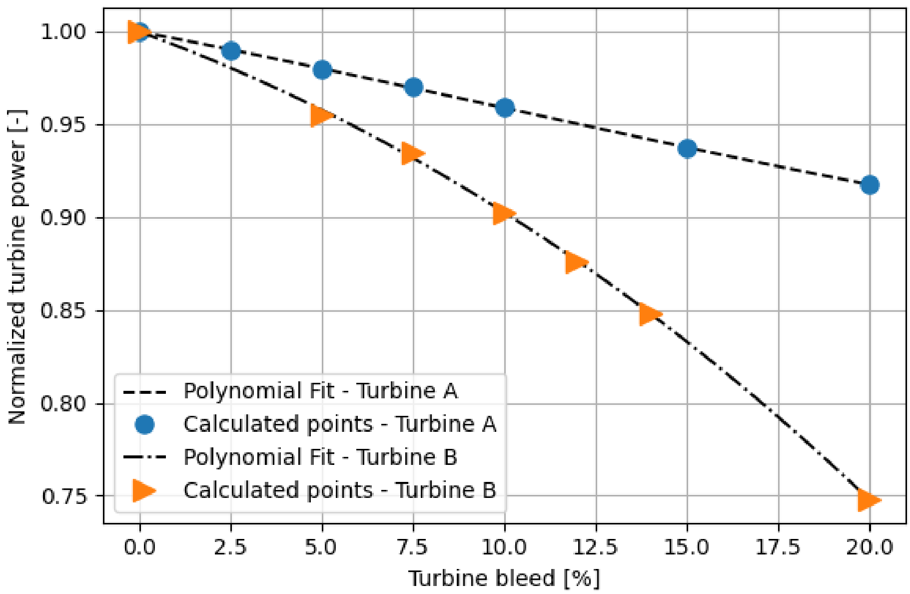


**Fig. 8.** Normalized power in turbines.

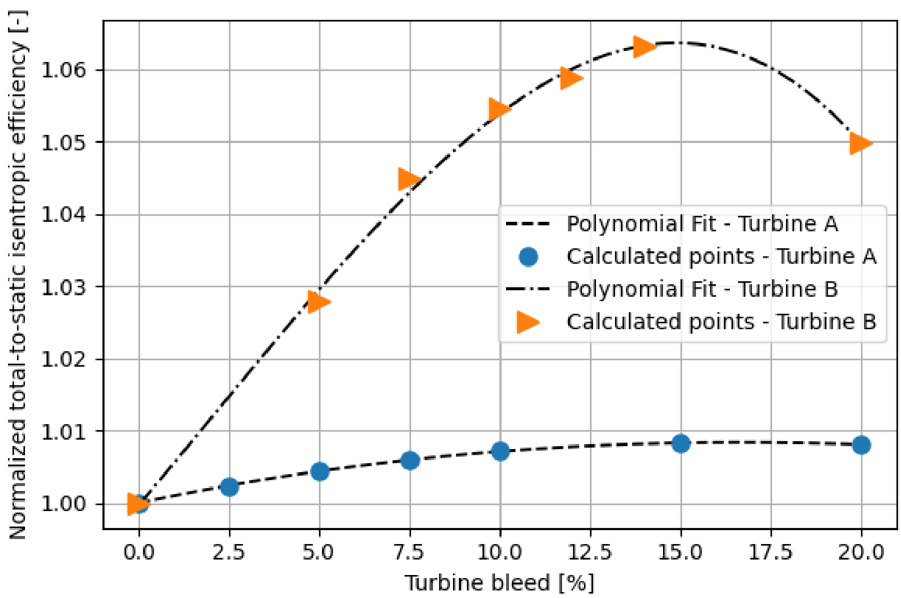


**Fig. 9.** Normalized total-to-static efficiency in turbines.

Fig. 10 shows the normalized stage power in turbine A. In the result figure, the dashed line represents results obtained with stage 1 of turbine A, and the dashed-dot line represents the results with stage 2 of turbine A. A slight increase in the power of the first stage is attributed to a change in the operating parameters of the medium and a small local pressure reduction, which enables a greater enthalpy drop to be utilized. Conversely, the significant decrease in power of the second stage primarily results from a lower mass flow of the working medium through this stage.

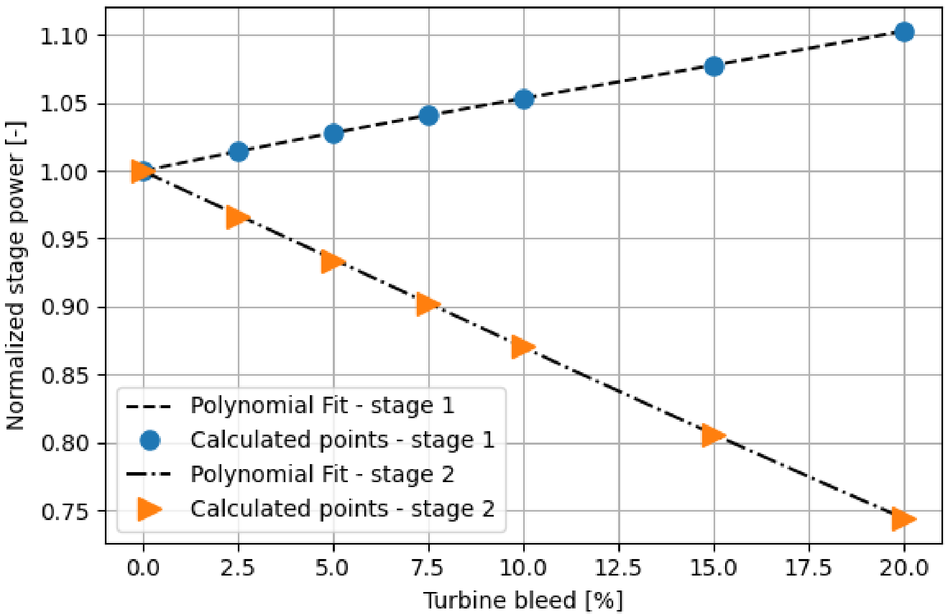


**Fig. 10.** Normalized stage power in turbine A.

The normalized stage power in turbine B is shown in Fig. 11. A similar trend is evident, as observed in the case of a two-stage turbine (turbine A), where the stages prior to the bleeder exhibit a slight increase in power or maintain a similar level as the bleed level increases. Conversely, the power in stages 4 and 5 decreases by up to nearly 50% and 60%, respectively, with a 20% reduction of the mass flow.

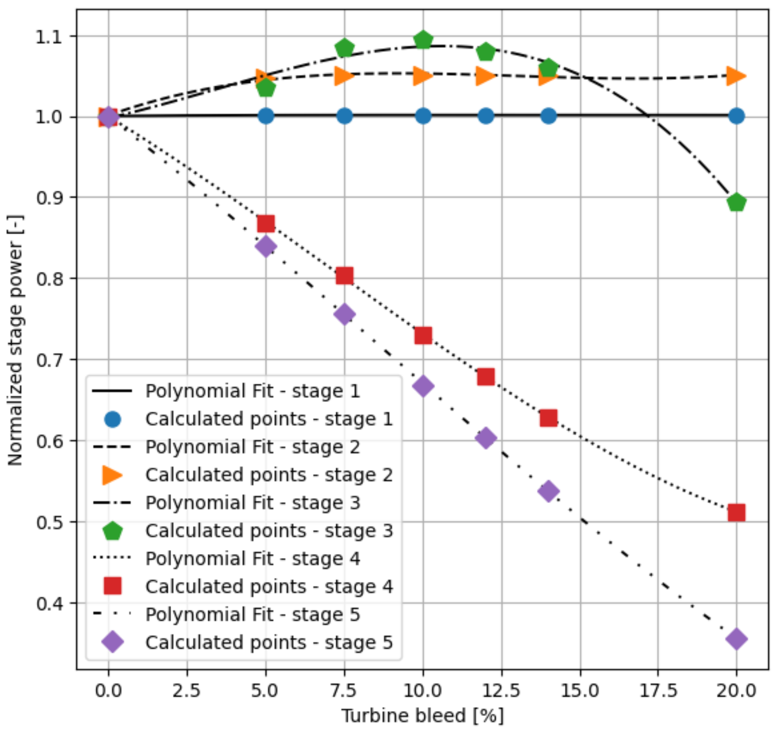


**Fig. 11.** Normalized stage power in turbine B.

### 4.2. Performance analysis under different outlet pressure conditions

In Fig. 12-Fig. 15, the impact of turbine outlet pressure on various aspects of turbine A is presented. These aspects include the overall power of turbine A, the power across its individual stages, its efficiency, and the power ratio. It is observed that as the outlet pressure increases, turbine A's power decreases almost linearly at all bleed levels. A similar trend is noted in the case of second-stage power. At the design point, turbine A's efficiency is the lowest when operating with a bleeder; however, it achieves higher efficiency values under broader characteristics (increasing outlet pressure) without a bleeder. The power ratio, defined as the ratio of second-stage power to first-stage power, tends to decrease. Without bleed at the design point, this power ratio is approximately 1.1, dropping to 0.5 at an outlet pressure of 30 kPa. Even lower values are recorded when the turbine operates with a 10%, 15%, and 20% reduction. At the highest bleed level and an outlet pressure of 30 kPa, the power ratio approaches 0.2. This value is critically important for structural design and the selection of turbine bearings.

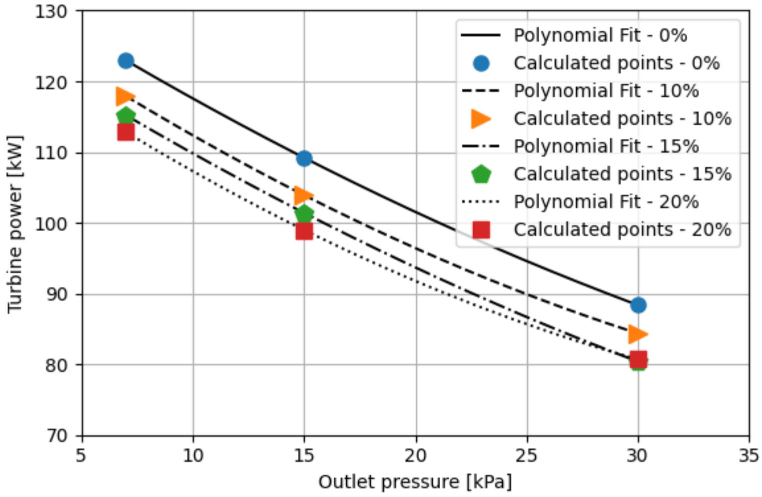


**Fig. 12.** Turbine power versus outlet pressure in turbine A for a different bleed level.

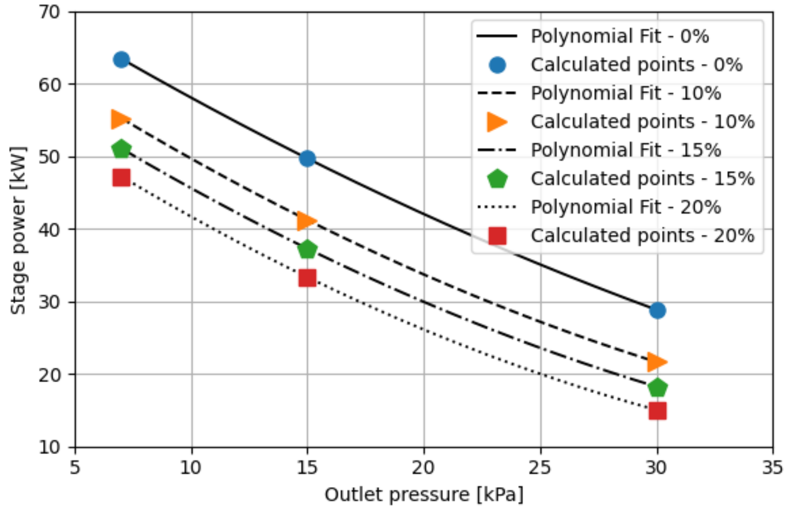


**Fig. 13.** Stage power versus outlet pressure in second stage in turbine A for a different bleed level.

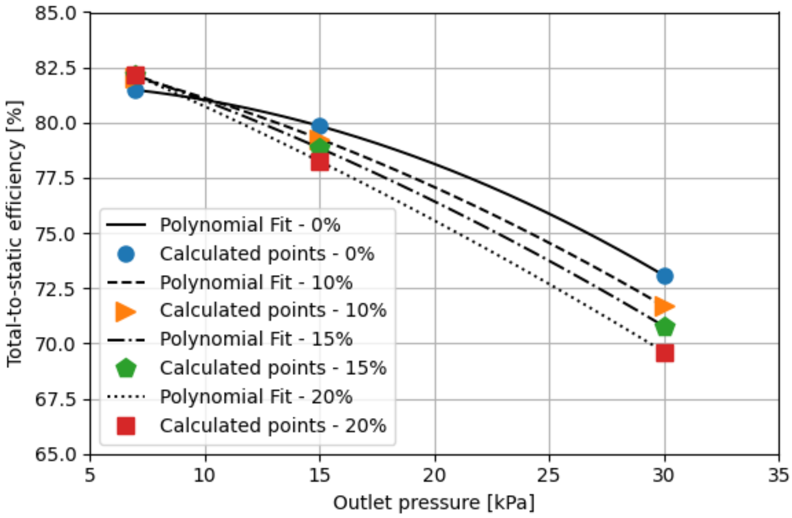


**Fig. 14.** Total-to-static efficiency versus outlet pressure in turbine A for a different bleed level.

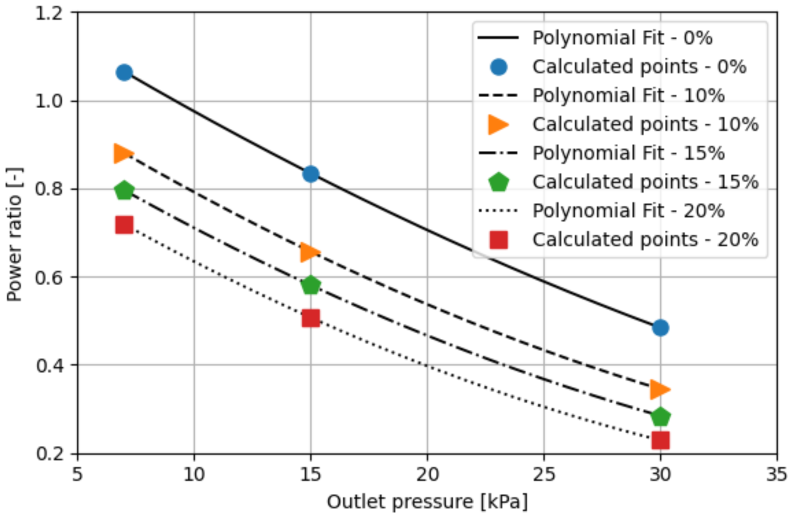


**Fig. 15.** Power ratio (second stage to first stage) versus outlet pressure in turbine A for a different bleed level.

### 4.3. Performance analysis under different rotational speed conditions

The impact of rotational speed on the efficiency, power, and power ratio of the turbine is depicted in Fig. 16-Fig. 18. An increase in nominal speed leads to higher efficiency in all analyzed cases. However, unlike the scenario where the influence of outlet pressure was analyzed, the turbine operating without a bleeder does not achieve significantly higher efficiency values. The increases in power and changes in power ratio are nearly identical across all cases. Notably, the variation in power ratio is marginal.

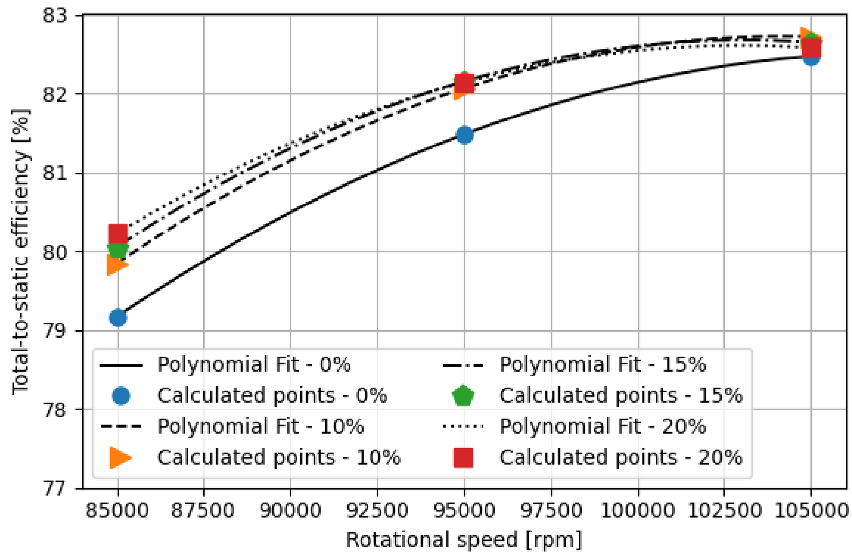


**Fig. 16.** Total-to-static efficiency versus rotational speed in turbine A for a different bleed level.

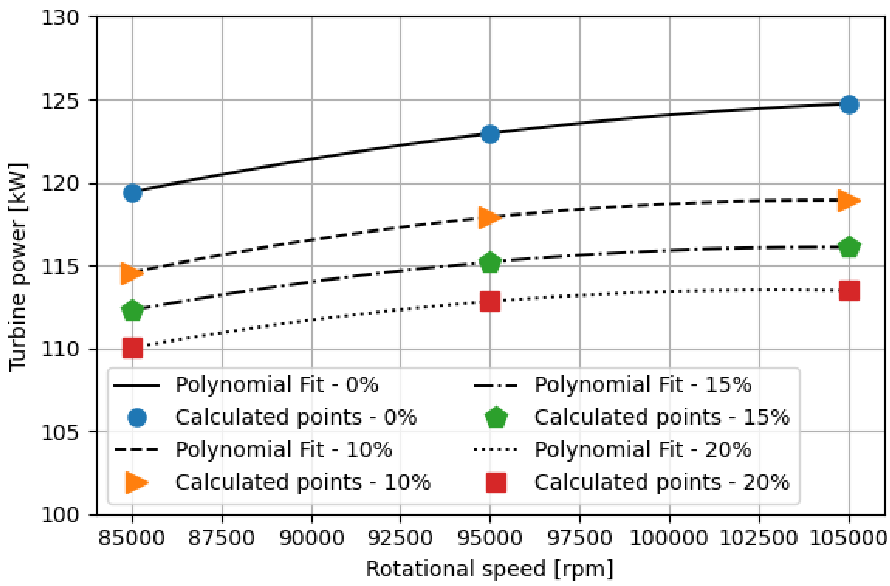


**Fig. 17.** Turbine power versus rotational speed in turbine A for a different bleed level.

Furthermore, the power and efficiency of turbines A and B were compared (Fig. 19-Fig. 20). At the nominal speed, turbine A achieved significantly higher efficiency (81.5%) and, consequently, higher power (122.9 kW). However, when operating at turbine B's nominal speed of 40 000 rpm, turbine A's efficiency drops to 51.7%, which is lower than turbine B's efficiency of 62.3%. In both turbines, an increase in rotational speed results in an increase in efficiency and power. Finally, the power ratio of turbine A as a function of its rotational speed is also presented (Fig. 21). At a speed of 40 000 rpm, the power ratio reaches 1.22, whereas at 105 000 rpm, it decreases to 1.06

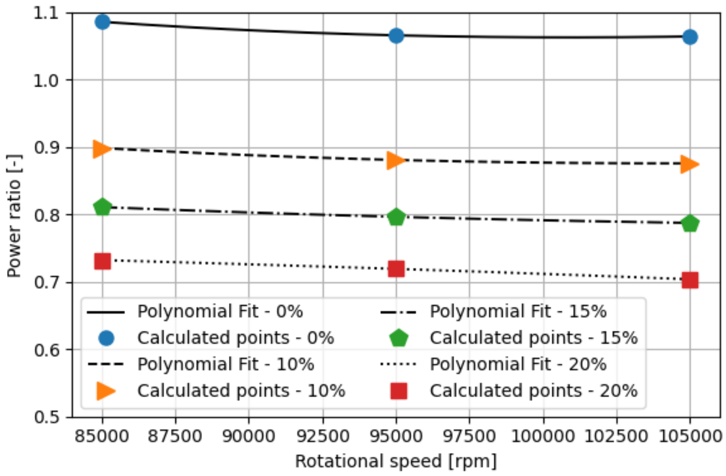


**Fig. 18.** Power ratio (second stage to first stage) versus rotational speed in turbine A for a different bleed level.

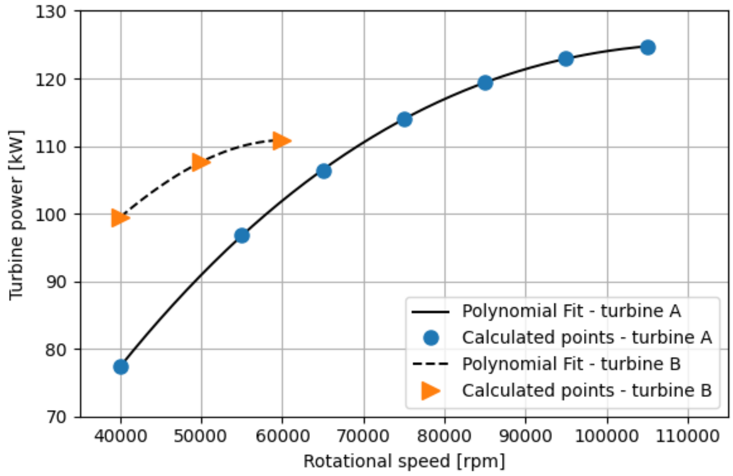


**Fig. 19.** Turbine power versus rotational speed in turbines.

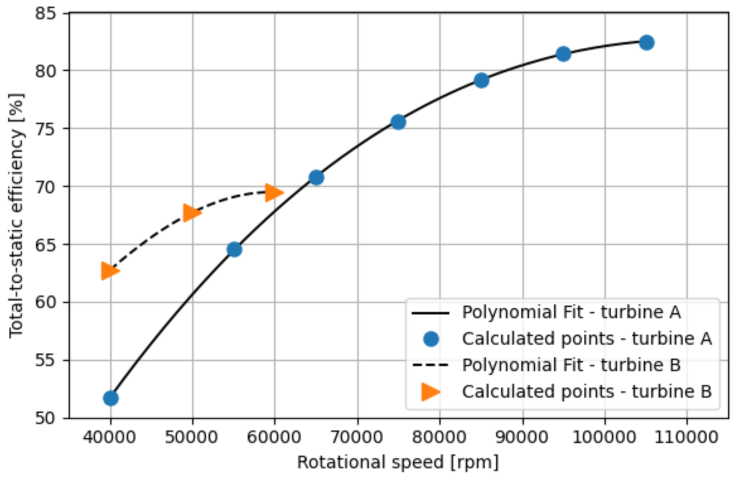


**Fig. 20.** Total-to-static efficiency versus rotational speed in turbines.

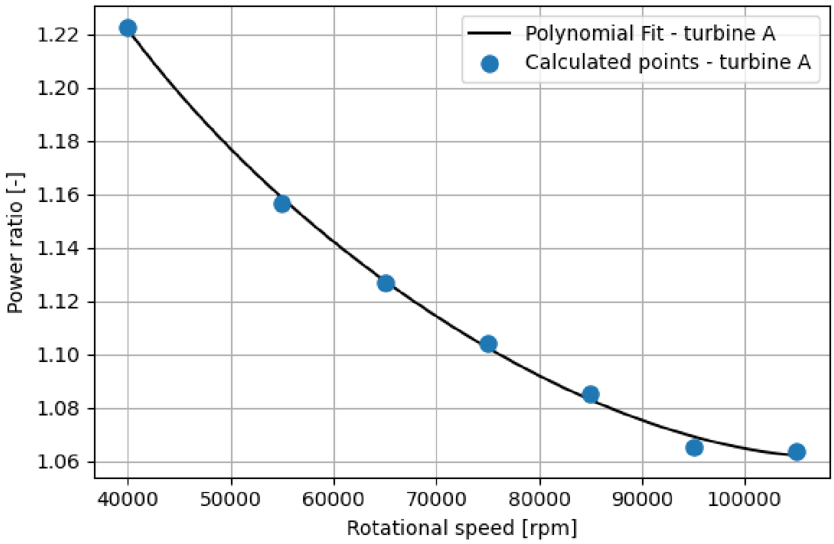


**Fig. 21.** Power ratio (second stage to first stage) versus rotational speed in turbine A.

It is worth mentioning at this point that similar power outputs as shown in Figure 18 have been analyzed for other biomass systems. In particular, the literature describes the case of 250 kWe, where it was assumed to use such solutions as: 1) gasification and reciprocating engine; 2) gasification and reciprocating engine, with low grade heat extracted from water jacket [50].

### 4.4. Detailed analysis

The flow through the channels is characterized by detachment of the stream, at the suction part of the blade, as illustrated in the entropy contours in Fig. 22-Fig. 23. Additionally, a high entropy region at the trailing edge appears in rotor stage 2 (Fig. 23). This region is the main source of losses in the analyzed flow. Therefore, it requires further design and optimization work aimed at reducing profile losses and trailing edge losses across a wide range of flow characteristics. Successful optimization of turbines operating in condensing and cogeneration modes was achieved in previous research [51]. This optimization utilized a Pareto front approach, providing a comprehensive overview of potential solutions and enabling the attainment of measurable benefits.

The velocity vectors  for various bleeder operating conditions are illustrated in Fig. 24-Fig. 26 . A notable area of fluid mixing is observed, resulting from the oversized dimensions of the bleeder, particularly when operating the second stage of the turbine at significantly lower loads. Future research can include a transient analysis of the medium flow through the turbine, focusing on the changing flow through the bleeder. However, this CFD analysis gives information about the nature of the flow and the direction of further action particularly relevant to new technical solutions whether for nCO2PP cycle [19] or other unusual turbines such as two-phase reaction turbine [52] and radial inflow turbine for ocean thermal energy [53].

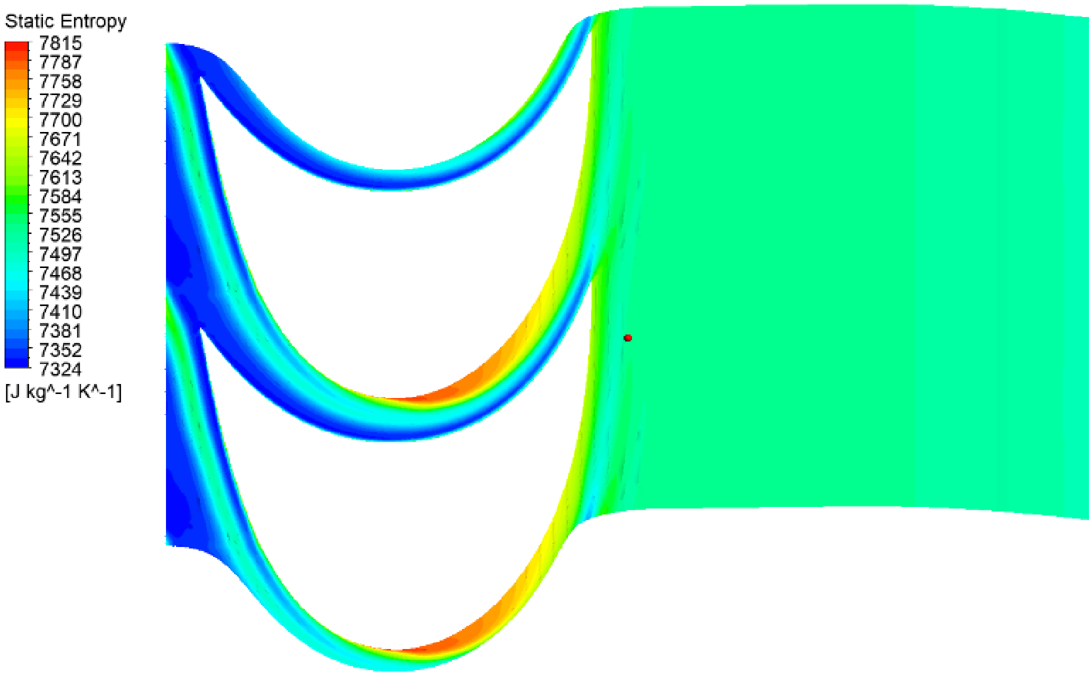


**Fig. 22** Static entropy contours in the stage 1 rotor at the mid span (operating in a mode with 20% of mass bleed).

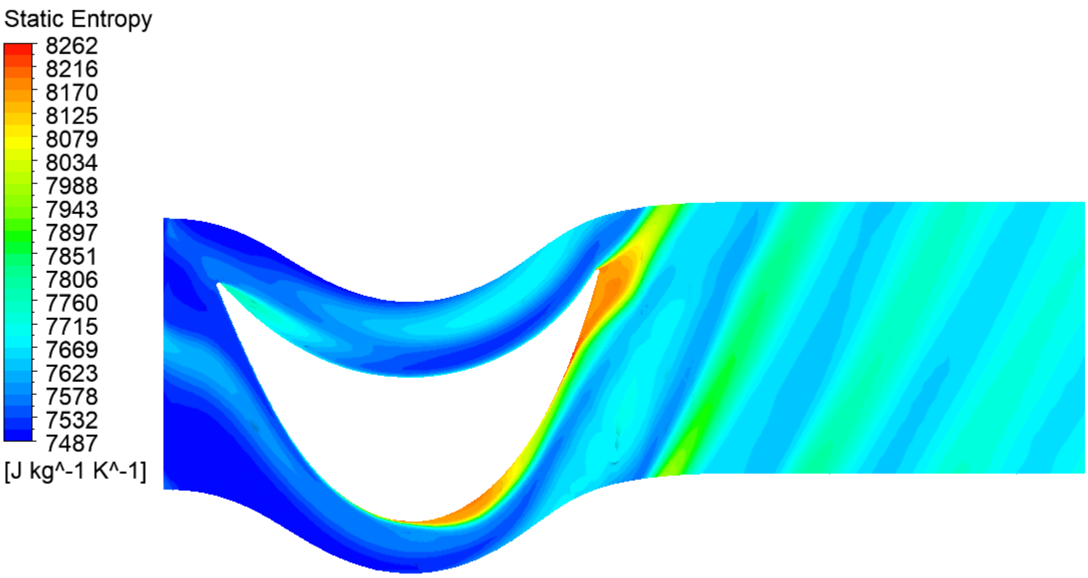


**Fig. 23** Static entropy contours in the stage 2 rotor at the mid span (operating in a mode with 20% of mass bleed).

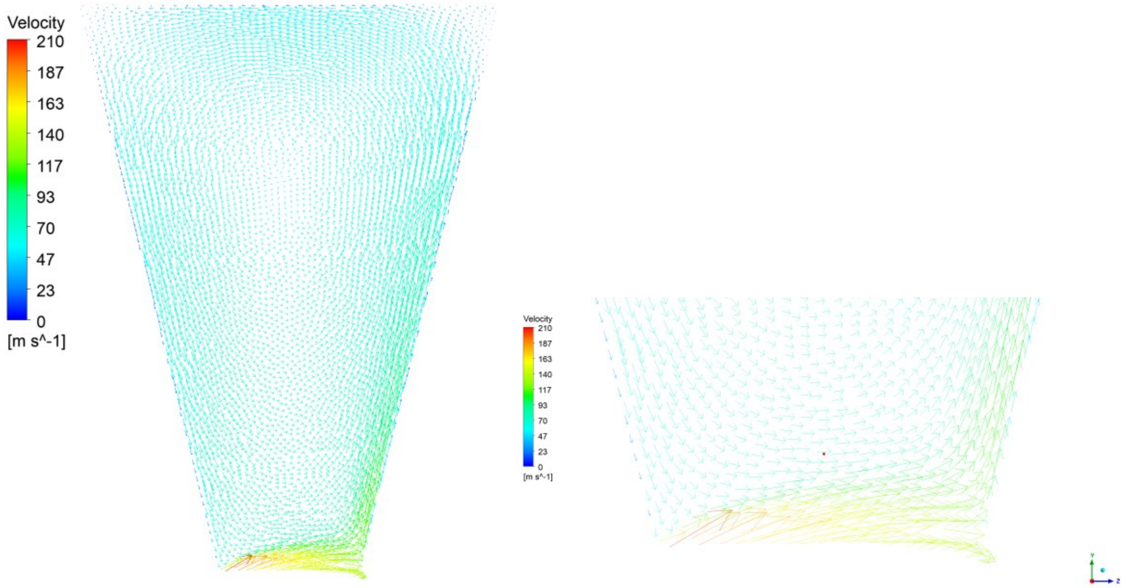


**Fig. 24** Velocity contours in bleed domain without mass flow output.

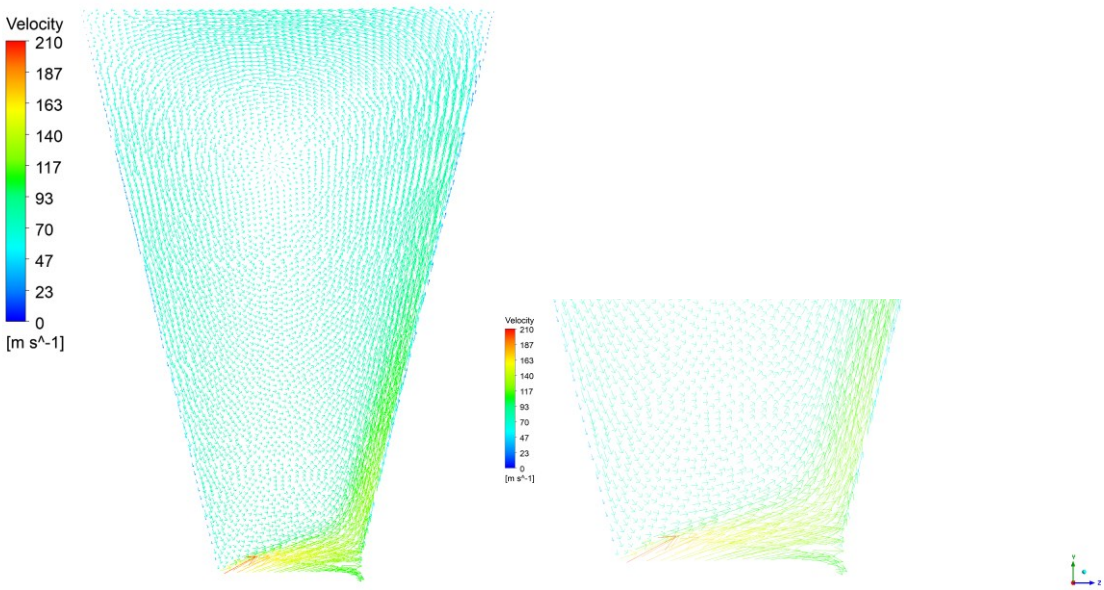


**Fig. 25** Velocity contours in bleed domain with 10% of mass flow.

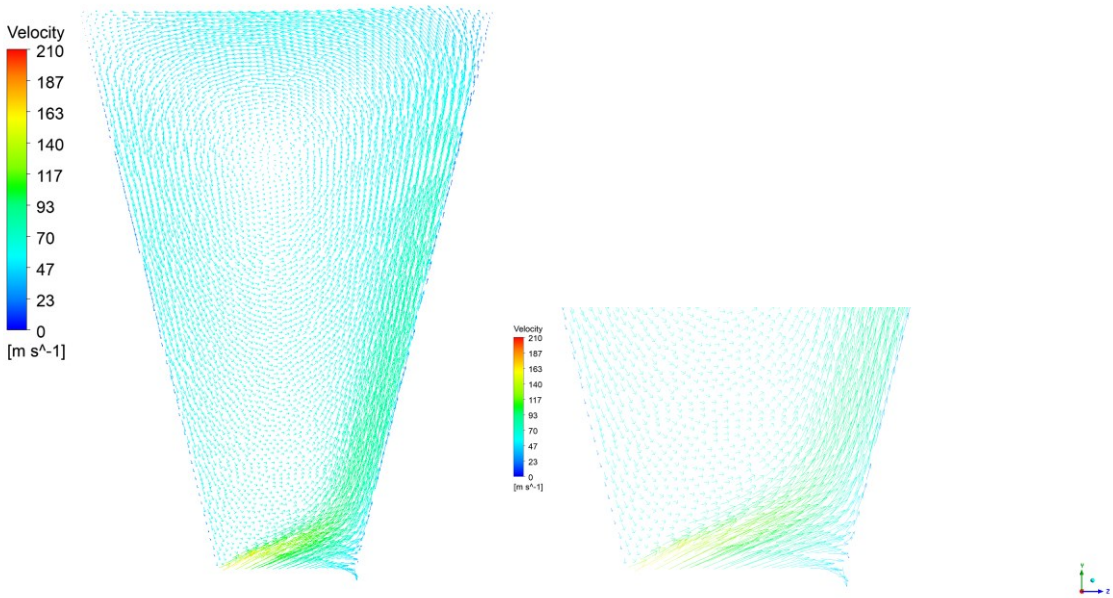


**Fig. 26** Velocity contours in bleed domain with 20% of mass flow.

## 5. Conclusions and perspectives

This work marks a significant stride in advancing high-speed, high-temperature turbine technology for innovative energy systems, specifically the negative carbon dioxide gas power plant ($nCO_2PP$). By meticulously designing and comparing two distinct turbine configurations, this study illuminates the critical role of bleed pressure and rotational speed in optimizing turbine performance.

The exploration of turbines A and B, differing in a number of stages and rotational speeds but sharing similar inlet and outlet dimensions, reveals nuanced insights into turbine efficiency and power dynamics. Particularly, it demonstrates how turbine A, despite higher base efficiency, encounters a drop in performance at turbine B's nominal speed, underscoring the delicate balance between speed, efficiency, and power output.

The core and at the same time most important findings relate to two facts, namely:

1) The superior controllability of the two-stage turbine is evidenced by the wide range (from 60 000 to 105 000 rpm) of high efficiencies (above 70%, up to an efficiency peak of 81.5%);

2) The two-stage turbine is also less influenced by bleed, which in the case of a five-stage turbine is characterized by a loss of power in the fourth and fifth stages along with the enthalpy not being worked out and thus achieving a higher losses at the turbine exit.

In order to achieve higher efficiency, it is anticipated that the blade channel shape, the number of blades, and the rotational speed will be optimized for several operating points. As evidenced by the above article, such a optimization is essential for achieving high efficiency values across a wide range of operating characteristics for both the turbine and the entire system.

## Acknowledgements

The research leading to these results has received funding from the Norway Grants 2014-2021 via the National Centre for Research and Development.

Article has been prepared within the frame of the project: "Negative CO2 emission gas power plant” - NOR/POLNORCCS/NEGATIVE-CO2-PP/0009/2019-00 which is co-financed by programme “Applied research” under the Norwegian Financial Mechanisms 2014-2021 POLNOR CCS 2019 - Development of CO2 capture solutions integrated in power and industry processes.

Part of calculations were carried out at the Academic Computer Centre in Gdańsk.

## References


[1] NASA Goddard Institute for Space Studies, GISTEMP Team, 2023: GISS Surface Temperature Analysis (GISTEMP), version 4 (2023). data.giss.nasa.gov/gistemp/.

[2] N.J.L. Lenssen, G.A. Schmidt, J.E. Hansen, M.J. Menne, A. Persin, R. Ruedy, et al., Improvements in the GISTEMP Uncertainty Model, J. Geophys. Res. Atmos. 124 (2019) 6307–6326. doi:10.1029/2018JD029522.

[3] O. Omoyele, M. Hoffmann, M. Koivisto, M. Larra, J.M. Weinand, J. Lin, et al., Increasing the resolution of solar and wind time series for energy system modeling : A review, 189 (2024). doi:10.1016/j.rser.2023.113792.

[4] E. Loth, Wind energy value and deep decarbonization design , what ' s next ?, Next Energy. 1 (2023) 100059. doi:10.1016/j.nxener.2023.100059.

[5] R. Daxini, Y. Wu, Review of methods to account for the solar spectral influence on photovoltaic device performance, Energy. 286 (2024) 129461. doi:10.1016/j.energy.2023.129461.

[6] U. Tesio, E. Guelpa, V. Verda, G. Manc, A review on multi energy systems modelling and optimization, 236 (2024). doi:10.1016/j.applthermaleng.2023.121871.

[7] W.M. Tefera, K.S. Kasiviswanathan, A global-scale hydropower potential assessment and feasibility evaluations, Water Resour. Econ. 38 (2022) 100198. doi:https://doi.org/10.1016/j.wre.2022.100198.

[8] C. Forman, I.K. Muritala, R. Pardemann, B. Meyer, Estimating the global waste heat potential, Renew. Sustain. Energy Rev. 57 (2016) 1568–1579. doi:10.1016/j.rser.2015.12.192.

[9] S. Alshammari, S.T. Kadam, Z. Yu, Assessment of single rotor expander-compressor device in combined organic Rankine cycle (ORC) and vapor compression refrigeration cycle (VCR), Energy. 282 (2023) 128763. doi:10.1016/j.energy.2023.128763.

[10] L. Wang, X. Bu, H. Li, Multi-objective optimization and off-design evaluation of organic rankine cycle (ORC) for low-grade waste heat recovery, Energy. 203 (2020) 117809. doi:10.1016/j.energy.2020.117809.

[11] D. Mikielewicz, J. Wajs, P. Ziółkowski, J. Mikielewicz, Utilisation of waste heat from the power plant by use of the ORC aided with bleed steam and extra source of heat, Energy. 97 (2016) 11–19. doi:10.1016/j.energy.2015.12.106.

[12] T. Ho, S.S. Mao, R. Greif, Comparison of the Organic Flash Cycle (OFC) to other advanced vapor cycles for intermediate and high temperature waste heat reclamation and solar thermal energy, Energy. 42 (2012) 213–223. doi:10.1016/j.energy.2012.03.067.

[13] D. Mikielewicz, Method and system for heat regeneration in a thermodynamic cycle with rapid expansion of steam (Organic Flash Cycle), patent No. PL237871, 2016.

[14] K. Adamson, T. Gordon, J.K. Carson, Q. Chen, F. Schlosser, L. Kong, et al., High-temperature and transcritical heat pump cycles and advancements : A review, Renew. Sustain. Energy Rev. 167 (2022) 112798. doi:10.1016/j.rser.2022.112798.

[15] A. Marina, S. Spoelstra, H.A. Zondag, A.K. Wemmers, An estimation of the European industrial heat pump market potential, Renew. Sustain. Energy Rev. 139 (2021) 110545. doi:10.1016/j.rser.2020.110545.

[16] P. Carroll, M. Chesser, P. Lyons, Air Source Heat Pumps field studies : A systematic literature review, Renew. Sustain. Energy Rev. 134 (2020) 110275. doi:10.1016/j.rser.2020.110275.

[17] A.A. Mana, S.I. Kaitouni, T. Kousksou, A. Jamil, Enhancing sustainable energy conversion: Comparative study of superheated and recuperative ORC systems for waste heat recovery and geothermal applications, with focus on 4E performance, Energy. 284 (2023) 128654. doi:10.1016/j.energy.2023.128654.

[18] Negative CO2 emission gas power plant, (2019). https://nco2pp.mech.pg.gda.pl/ (accessed May 10, 2024).

[19] P. Ziółkowski, K. Stasiak, M. Amiri, D. Mikielewicz, Negative carbon dioxide gas power plant integrated with gasification of sewage sludge, Energy. 262 (2023). doi:10.1016/j.energy.2022.125496.

[20] M. Uddin, H. Gurgenci, A. Klimenko, Z. Guan, Heat transfer analysis of supercritical CO2 in a High-Speed turbine rotor shaft cooling passage, Therm. Sci. Eng. Prog. 39 (2023) 101694. doi:10.1016/j.tsep.2023.101694.

[21] G. Xu, G. Zhao, Y. Quan, R. Liang, T. Li, B. Dong, et al., Design and optimization of a radial-axial two-stage coaxial turbine for high-temperature supercritical organic Rankine cycle, Appl. Therm. Eng. 227 (2023) 120365. doi:10.1016/j.applthermaleng.2023.120365.

[22] M. Banaszkiewicz, Numerical investigations of crack initiation in impulse steam turbine rotors subject to thermo-mechanical fatigue, Appl. Therm. Eng. 138 (2018) 761–773. doi:10.1016/j.applthermaleng.2018.04.099.

[23] U. Unnikrishnan, V. Yang, A review of cooling technologies for high temperature rotating components in gas turbine, Propuls. Power Res. 11 (2022) 293–310. doi:10.1016/j.jppr.2022.07.001.

[24] R.H. Tindell, T.M. Alston, C.A. Sarro, G.C. Stegmann, L. Gray, J. Davids, Computational Fluid Dynamics Analysis of a Steam Power Plant Low-Pressure Turbine Downward Exhaust Hood, J. Eng. Gas Turbines Power. 118 (1996) 214–224. doi:10.1115/1.2816543.

[25] P. Ziółkowski, S. Głuch, T. Kowalczyk, J. Badur, Revalorisation of the Szewalski's concept of the law of varying the last-stage blade retraction in a gas-steam turbine, E3S Web Conf. 323 (2021) 00034. doi:10.1051/e3sconf/202132300034.

[26] K. Veerabathraswamy, A. Senthil Kumar, Effective boundary conditions and turbulence modeling for the analysis of steam turbine exhaust hood, Appl. Therm. Eng. 103 (2016) 773–780. doi:10.1016/j.applthermaleng.2016.04.126.

[27] Z. Burton, G.L. Ingram, S. Hogg, A Literature Review of Low Pressure Steam Turbine Exhaust Hood and Diffuser Studies, J. Eng. Gas Turbines Power. 135 (2013). doi:10.1115/1.4023611.

[28] P. Ziółkowski, Ł. Witanowski, P. Klonowicz, S. Głuch, Optimization of the last stage of gas-steam turbine using a hybrid method, in: Proc. 14th Eur. Conf. Turbomach. Fluid Dyn. Thermodyn., Gdańsk, 2021: pp. 1–12.

[29] P. Lampart, Ł. Witanowski, P. Klonowicz, Efficiency Optimisation of Blade Shape in Steam and ORC Turbines, Mech. Mech. Eng. 22 (2018) 553–564. doi:10.2478/mme-2018-0044.

[30] P. Klonowicz, Ł. Witanowski, T. Suchocki, Ł. Jędrzejewski, P. Lampart, Selection of optimum degree of partial admission in a laboratory organic vapour microturbine, Energy Convers. Manag. 202 (2019). doi:10.1016/j.enconman.2019.112189.

[31] Ł. Witanowski, P. Klonowicz, P. Lampart, T. Suchocki, Ł. Jędrzejewski, D. Zaniewski, et al., Optimization of an axial turbine for a small scale ORC waste heat recovery system, Energy. 205 (2020) 118059. doi:10.1016/j.energy.2020.118059.

[32] P. Ziółkowski, J. Badur, H. Pawlak- Kruczek, K. Stasiak, M. Amiri, L. Niedzwiecki, et al., Mathematical modelling of gasification process of sewage sludge in reactor of negative CO2 emission power plant, Energy. 244 (2022) 122601. doi:10.1016/j.energy.2021.122601.

[33] P. Ziółkowski, P. Madejski, M. Amiri, T. Kuś, K. Stasiak, N. Subramanian, et al., Thermodynamic analysis of negative CO2 emission power plant using aspen plus, aspen Hysys, and ebsilon software, Energies. 14 (2021) 1–27. doi:10.3390/en14196304.

[34] M. Kaszuba, P. Ziółkowski, D. Mikielewicz, Comparative study of oxygen separation using cryogenic and membrane techniques for nCO2PP, 36th Int. Conf. Effic. Cost, Optim. Simul.

Environ. Impact Energy Syst. ECOS 2023. (2023) 2903–2914. doi:10.52202/069564-0260.

[35] K. Stasiak, I.S. Ertesvåg, P. Ziólkowski, D. Mikielewicz, Exergetic Analysis of the nCO2PP Cycle with Particular Reference to the Exergy Destruction of Sewage Sludge Due to Gasification, in: 36th Int. Conf. Effic. Cost, Optim. Simul. Environ. Impact Energy Syst. (ECOS 2023), ECOS 2023, Las Palmas De Gran Canaria, Spain, 2023: pp. 222–232. doi:10.52202/069564-0021.

[36] M. Kaszuba, P. Ziółkowski, D. Mikielewicz, Performance of cryogenic oxygen production unit with exhaust gas bleed for sewage sludge gasification and different oxygen purities, Arch. Thermodyn. 44 (2023) 1–19. doi:10.24425/ather.2023.14xxxx.

[37] K. Stasiak, P. Ziółkowski, D. Mikielewicz, Selected Aspects of Performance of Organic Rankine Cycles Incorporated Into Bioenergy With Carbon Capture and Storage Using Gasification of Sewage Sludge, J. Energy Resour. Technol. 146 (2024). doi:10.1115/1.4064196.

[38] I.S. Ertesvåg, P. Madejski, P. Ziółkowski, D. Mikielewicz, Exergy analysis of a negative CO2 emission gas power plant based on water oxy-combustion of syngas from sewage sludge gasification and CCS, Energy. 278 (2023) 127690. doi:10.1016/j.energy.2023.127690.

[39] G. Cordes, W. Traupel, Die Theorie der Strömung durch Radialmaschinen. VIII + 160 S. m. 103 Abb. Karlsruhe 1962. Verlag G. Braun. Preis geb. DM 27,—, ZAMM - Zeitschrift Für Angew. Math. Und Mech. 43 (1963). doi:10.1002/zamm.19630430310.

[40] P. Klonowicz, F. Heberle, M. Preißinger, D. Brüggemann, Significance of loss correlations in performance prediction of small scale, highly loaded turbine stages working in Organic Rankine Cycles, Energy. 72 (2014) 322–330.

[41] H. Brenner, Navier–Stokes revisited, Phys. A Stat. Mech. Its Appl. 349 (2005) 60–132. doi:10.1016/j.physa.2004.10.034.

[42] O. Reynolds, On the Equation of Motion and the Boundary Conditions for Viscous Fluid, Fluid, Br. Assoc. Sec. A Pap. II. 46 (1883) 132–137.

[43] J. Badur, M. Feidt, P. Ziółkowski, Neoclassical Navier–Stokes Equations Considering the Gyftopoulos–Beretta Exposition of Thermodynamics, Energies. 13 (2020) 1656. doi:10.3390/en13071656.

[44] P. Radomski et al Computational fluid dynamics simulation of heat transfer from densely packed gold nanoparticles to isotropic media, Arch. Thermodyn. (2023). doi:10.24425/ather.2021.138111.

[45] ANSYS®, Academic Research Mechanical and CFD, Release 23.2, (2023).

[46] E.W. Lemmon, I.H. Bell, M.L. Huber, M.O. McLinden, NIST Standard Reference Database 23: Reference Fluid Thermodynamic and Transport Properties-REFPROP, Version 10.0, National Institute of Standards and Technology, (2018). doi:https://doi.org/10.18434/T4/1502528.

[47] P. Klonowicz, A. Borsukiewicz-Gozdur, P. Hanausek, W. Kryłłowicz, D. Brüggemann, Design and performance measurements of an organic vapour turbine, Appl. Therm. Eng. 63 (2014) 297–303. doi:10.1016/j.applthermaleng.2013.11.018.

[48] A. Andrearczyk, P. Bagiński, P. Klonowicz, Numerical and experimental investigations of a turbocharger with a compressor wheel made of additively manufactured plastic, Int. J. Mech. Sci. 178 (2020). doi:10.1016/j.ijmecsci.2020.105613.

[49] P. Ziółkowski, Ł. Witanowski, S. Głuch, P. Klonowicz, M. Feidt, A. Koulali, Example of Using Particle Swarm Optimization Algorithm with Nelder–Mead Method for Flow Improvement in Axial Last Stage of Gas–Steam Turbine, Energies . 17 (2024). doi:10.3390/en17122816.

[50] P. Thornley, J. Rogers, Y. Huang, Quantification of employment from biomass power plants, Renew. Energy. 33 (2008) 1922–1927. doi:10.1016/j.renene.2007.11.011.

[51] Ł. Witanowski, P. Klonowicz, P. Lampart, P. Ziółkowski, Multi-objective optimization of the

ORC axial turbine for a waste heat recovery system working in two modes: cogeneration and condensation, Energy. 264 (2023) 126187. doi:10.1016/j.energy.2022.126187.

[52] H. Li, S. Rane, Z. Yu, Investigation of the performance and flow characteristics of two-phase reaction turbines in total flow geothermal systems, Renew. Energy. 175 (2021) 345–372. doi:10.1016/j.renene.2021.05.022.

[53] Y. Chen, Y. Liu, W. Liu, Y. Ge, Y. Xue, L. Zhang, Optimal design of radial inflow turbine for ocean thermal energy conversion based on the installation angle of nozzle blade, Renew. Energy. 184 (2022) 857–870. doi:10.1016/j.renene.2021.12.016.